Geophysical Research Letters

RESEARCH LETTER
10.1029/2024GL108840

Effects of Dilatant Hardening on Fault Stabilization and Structural Development

S. A. Williams[1] and M. E. French[1]

[1]Rice University, Houston, TX, USA

Key Points:

- We measured the transition between dynamic and stable rupture as a result of dilatant hardening
- We observed differences in microstructural development tied to the shift in rupture style
- We developed a model of fracture nucleation and propagation at different pore fluid pressures

Supporting Information:

Supporting Information may be found in the online version of this article.

Correspondence to:

S. A. Williams,
stewart@rice.edu

Citation:

Williams, S. A., & French, M. E. (2024). Effects of dilatant hardening on fault stabilization and structural development. *Geophysical Research Letters*, *51*, e2024GL108840. https://doi.org/10.1029/2024GL108840

Received 14 FEB 2024
Accepted 18 APR 2024

Author Contributions:

Conceptualization: M. E. French
Data curation: S. A. Williams
Formal analysis: S. A. Williams
Funding acquisition: M. E. French
Investigation: S. A. Williams
Methodology: S. A. Williams
Project administration: M. E. French
Resources: M. E. French
Software: S. A. Williams
Supervision: M. E. French
Visualization: S. A. Williams
Writing – original draft: S. A. Williams
Writing – review & editing: S. A. Williams, M. E. French

Abstract Dilatant hardening is one proposed mechanism that causes slow earthquakes along faults. Previous experiments and models show that dilatant hardening can stabilize fault rupture and slip in several lithologies. However, few studies have systematically measured the mechanical behavior across the transition from dynamic to slow rupture or considered how the associated damage varies. To constrain the processes and scales of dilatant hardening, we conducted triaxial compression experiments on cores of Crab Orchard sandstone and structural analyses using micro-computed tomography imaging and petrographic analysis. Experiments were conducted at an effective confining pressure of ~10 MPa, while varying confining pressure (10–130 MPa) and pore fluid pressure (1–120 MPa). Above 15 MPa pore fluid pressure, dilatant hardening slows the rate of fault rupture and slip and deformation becomes more distributed amongst multiple faults as microfracturing increases. The resulting increase in fracture energy has the potential to control fault slip behavior.

Plain Language Summary When rocks are breaking, the pore spaces and developing fractures dilate, resulting in a decrease in pore fluid pressures. This decrease can strengthen the rock from ongoing deformation in a process known as dilatant hardening. We conducted experiments to better understand how this strengthening effect works, in particular looking at the ratio of pore fluid pressure to the external confining pressure (simulating rocks buried at depth), and also analyzed how the fractures that develop can vary from dilatant hardening. We found a threshold pressure at which the strengthening peaked, and increasing pore fluid pressure did not change how strong the rocks got from continuing deformation. We also observed a drastic increase in how damage was distributed due to this hardening effect at both a large (visible to the naked eye) and small scale (only visible in a high-magnification microscope). These results indicate that dilatant hardening can increase how much energy must be expended to break the rock and to cause faults to slip when pore fluid pressures are high enough, and likely plays a role in stabilizing fault slip, causing earthquakes to slow down and be less dynamic.

1. Introduction

During brittle deformation, fault formation and growth leads to dilation due to an increase in fracture and pore volume (Brace, 1978; Brace et al., 1966; Handin et al., 1963). This dilation can result in a decrease in the pore fluid pressure within and adjacent to the faults if the rate of dilation outpaces the rate of fluid flow (e.g., Brace, 1978; Brace et al., 1966; Frank, 1965). This process strengthens the fault by locally increasing the effective stress in a phenomenon known as "dilatant hardening" (Brace & Martin, 1968; Rice, 1975). During the stress drop associated with fault rupture and cohesion loss, this process has also been shown to slow the rupture and slip processes (Aben & Brantut, 2021; Brace & Martin, 1968; Brantut, 2020; French & Zhu, 2017). As a result, dilatant hardening has been proposed as a cause of slow modes of fault slip (Liu & Rubin, 2010; Ougier-Simonin & Zhu, 2013; Rudnicki, 1984; Segall et al., 2010), particularly during the loss of cohesion (French & Zhu, 2017).

For dilatant hardening to be effective at reducing the rate of rupture, strain rates must be fast enough relative to pore fluid diffusion into the rock and pore fluid pressures must be high enough to create a strengthening effect. Evidence for near-lithostatic pore fluid pressures in regions that exhibit slow modes of slip, low permeability rocks, and the possibility of cohesion gain between slip events makes dilatant hardening a strong candidate as the cause of slow earthquakes (Audet et al., 2009; Liu & Rice, 2007; Peacock et al., 2011; Shelly et al., 2006; Zhu et al., 2020). However, both the effectiveness of dilatant hardening at slowing rupture in different lithologies and evidence for it in the rock record are still unknown.

Here we present the first systematic study on the effects of dilatant hardening on the rate of cohesion loss and the resulting distribution of fracture damage associated with fault rupture. We study dilatant hardening in a

low-porosity, low-permeability homogeneous sandstone to evaluate first-order controls on the mechanics of the dilatant hardening process. We conducted fault rupture experiments over a broad range of pore fluid pressures and correlated failure behavior with fracture damage at micro- to macroscopic observational scales. Our results show that the ratio of pore fluid pressure to confining pressure controls both the stability of failure as well as the magnitude and distribution of fracturing, indicating an increase in shear fracture energy.

2. Materials and Methods

2.1. Sample Description

We performed triaxial compression experiments on the Pennsylvanian Crab Orchard sandstone from Tennessee, US. This sandstone is dominantly quartz (80%–90%) (Ceia et al., 2019; Churcher et al., 1991; Menéndez et al., 1996), which minimizes compositional complexity and heterogeneity that can cause sample-to-sample variability and impact fracture patterns. Bedding occurs as mm-scale cross-beds (Gehne & Benson, 2017), which we identified as minor compositional variations due to oxide concentrations.

Experimental specimens are cores 25.4 mm in diameter and 52 mm in length. Cores were prepared from a single block of sandstone and from the same bedding interval in an effort to minimize potential sample variability. All cores were prepared with bedding perpendicular to the long axis of the cores. We measured the initial connected porosity of each sample, ϕ, to be 3.5% ± 0.5%. We measured the permeability of the sandstone to be 1.3×10^{-17} m^2 and within the range reported values for the Crab Orchard sandstone (10^{-18} to 10^{-17} m^2) (Gehne & Benson, 2017).

2.2. Deformation Experiments

We conducted fault rupture and slip experiments on 13 intact sandstone cores using a standard triaxial deformation apparatus (Table S1 and Figure S1 in Supporting Information S1). The experiments are axial compression tests, whereby confining and pore fluid pressures are held constant and the axial piston is advanced at a constant rate until the sample fails by fault formation and subsequent slip. Each sample was deformed at an axial displacement rate of 0.011 μm/s (axial strain rate, $\dot{\varepsilon}_a$, of 2.35×10^{-7} s^{-1}) to 3.6% axial strain. To systematically evaluate the roles of fluid pressure on dilatant hardening and for comparison with previous studies, all experiments were conducted at an effective confining pressure ($\sigma_3' = \sigma_3 - P_f$) of 10 MPa but at varying magnitudes of confining (σ_3) and pore fluid (P_f) pressures. All experiments were conducted at room temperature (~23°C).

2.3. Structural Analyses

Damage due to dilatant hardening during fault nucleation and propagation was characterized at three scales: macroscale through hand sample observations, mesoscale using X-ray micro-computed tomography (μCT), and microscale using transmitted light microscopy. The samples chosen for imaging and structural analyses were deformed to similar axial strains (~3.6%) and pore fluid pressures between 1 and 120 MPa.

The faulted samples were both qualitatively and quantitatively described at the macroscale. We noted whether fractures appeared localized or distributed. We also counted fractures using a circumferential transect line at approximately the middle of each core and classified fractures as either major and minor. Major faults display visible offset along the fracture indicated by displacement at the ends of the core, bedding offset, or radial protrusion normal to the surface of the core.

Mesoscale 3D fracture patterns were characterized for seven cores using μCT images collected at the High Resolution X-ray Computed Tomography Facility at The University of Texas at Austin. We processed the data using *ImageJ*. We then isolated and measured the orientations of individual fractures and calculated the fracture surface area using *Autodesk Fusion 360* (Text S4 and Figures S3–S8 in Supporting Information S1).

The intensity and spatial distribution of microscale deformation was evaluated by measuring microcrack density and orientation on two cores that were also analyzed using μCT. One was faulted at high pore fluid pressure (G0165, 120 MPa) and the other low pore fluid pressure (G0163, 1 MPa). We measured local microcrack densities along a 20 × 9 point grid with grid points spaced 2.54 mm using transects spanning 1,000 μm across, centered on each grid point (Figure 1a). This method allows us to measure a representative number of microcracks, their spatial distribution relative to larger fractures, and their preferred orientation.

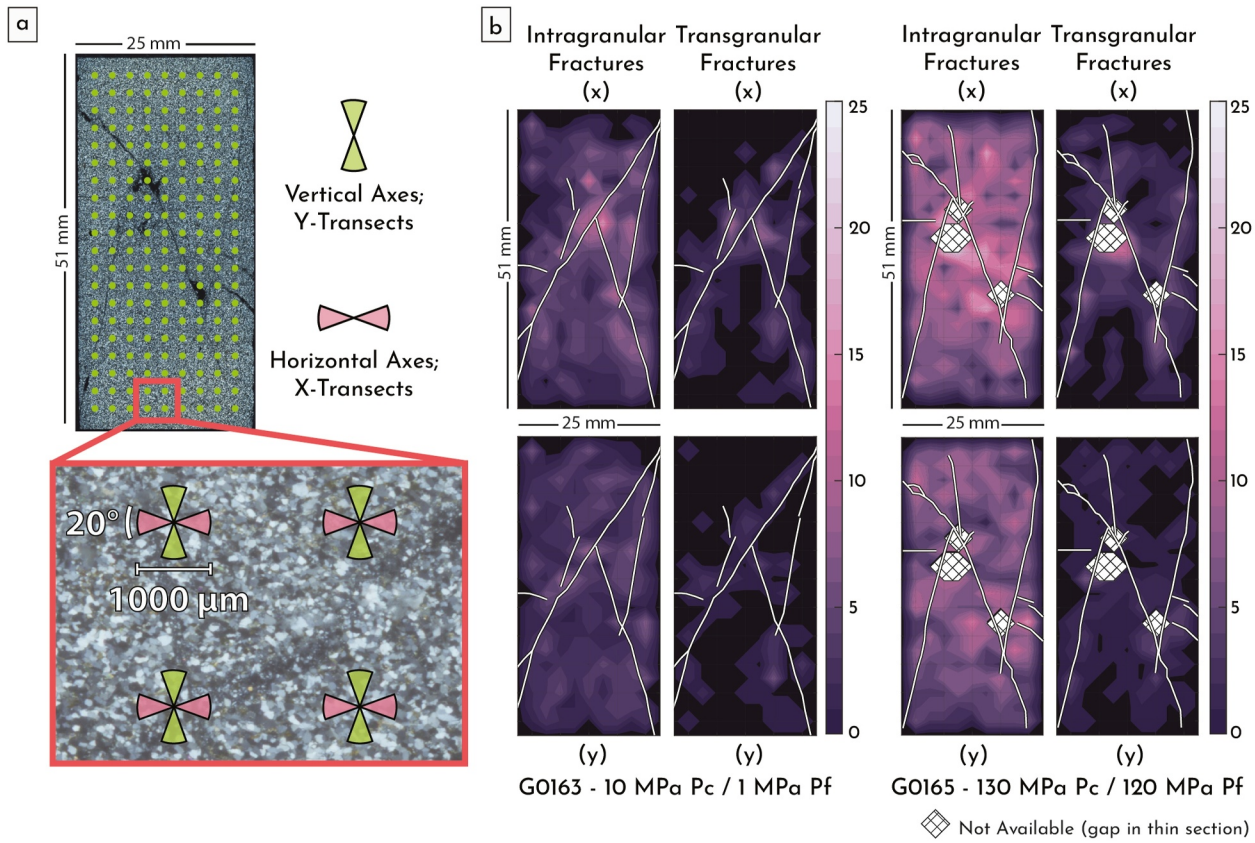

Figure 1. Methodology and results of microcrack density measurements. (a) Transmitted light photomicrograph of sample G0165 deformed at 120 MPa pore fluid pressure. Overlain is a 20 × 9 grid with a uniform 2.54 mm spacing (cyan dots); microcracks were counted along transects in the radial (x) and axial (y) directions centered along each grid point. We allowed for a 20° sweep of the stage, and therefore the transect line, to capture a larger area while still preserving the record of orientation differences. (b) Microcrack density map from samples faulted at low (G0163, 1 MPa) and high (G0165, 120 MPa) pore fluid pressures. Microcrack densities measured along radial and axial transects are shown separately.

3. Results

3.1. Mechanical Data

During faulting, strain-weakening occurred in multiple punctuated steps whereby periods of weakening were separated by periods of strain-neutral strength often indicative of frictional sliding, which we refer to as "apparent frictional sliding" (Figure 2). We observe a range of strain-weakening rates which we distinguish as "rapid" and "slow" stress drops during failure based on stress drop gradient. "Rapid" stress drops are dynamic, meaning the measured drop is controlled by the apparatus stiffness and inertia (Figures 2d and 2h). Slow stress drops occurred at rates between 10^{-6} and 10^{-1} MPa/s, and rapid stress drops occurred between 10^{-1} and 10^{5} MPa/s. Rapid stress drops were sometimes audible, but only when the stress drop was relatively large. No sound was observed during any of the slow stress drops. Because there are multiple periods of both rapid and slow stress drops in any given experiment, we quantify the cumulative sum of both within each experiment. We normalize the cumulative sum of rapid and slow stress drop to the total stress drop to account for variations in peak strengths when comparing experiments.

With increasing pore fluid pressure, the proportion of the total stress drop that is slow increases as the proportion that is rapid decreases (Figure 3a). The relationships between rapid and slow stress drops and pore fluid pressure are non-linear. As pore fluid pressure increases from 1 to 15 MPa, the rapid stress drops decrease from ∼70% to ∼20% of the total stress drop as slow stress drops increase from ∼30% to ∼80%. The degree to which this transition is gradual or abrupt is difficult to resolve. However, at higher pore fluid pressures (>15 MPa), further increasing pore fluid pressure does not systematically change the proportion of slow and rapid stress drops. For

10.1029/2024GL108840

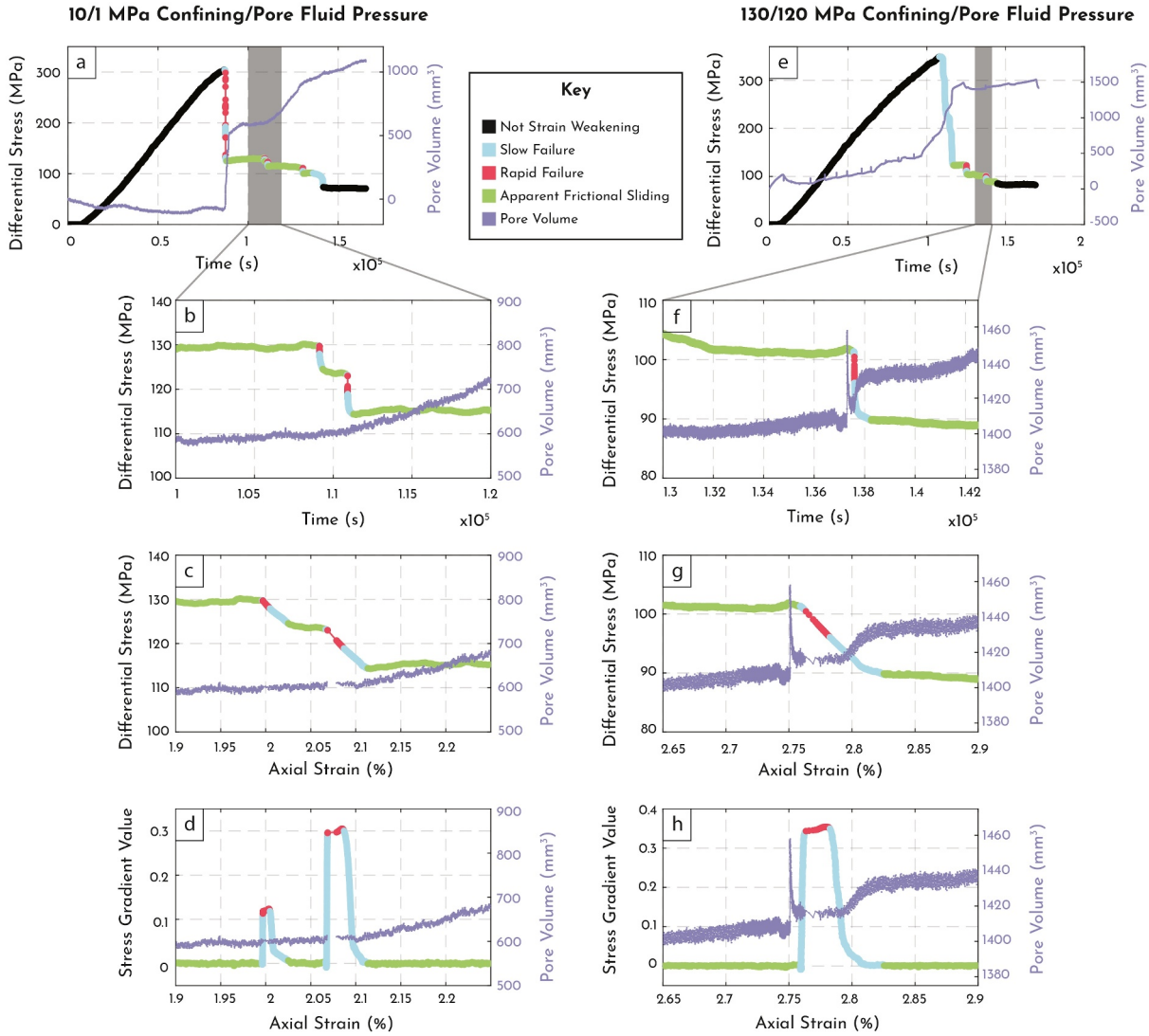

Figure 2. Mechanical data for representative experiments at low and high pore fluid pressures (a) An overview of the experiment comparing differential stress versus time, (b) A zoomed in segment of (a), as indicated by the gray bar, highlighting the relationship of minor stress drops with pore fluid volume, (c) The same segment but plotting differential stress as a function of axial strain, (d) The stress drop gradient plotted for the same segment and highlighting the method used for distinguishing rapid and slow failure modes. "Rapid" failure is identified as a plateau or near-constant stress drop gradient, (e–h) Are plots of the same parameters, but for experiment G0165, which was conducted at 130 MPa confining pressure and 120 MPa pore fluid pressure.

most experiments with pore pressure greater than 15 MPa, total strain-weakening is accommodated almost entirely through slow failure (Figure 3a).

We calculated the duration from peak strength to the end of the first measured rapid stress drop for each experiment to evaluate initial failure rate prior to the more complicated strain weakening behavior. At the onset of failure, we observe that higher pore fluid pressure correlates to an increase in the duration from peak strength to the end of the initial rapid stress drop. The rate of strain weakening during this period indicates the same: a substantial decrease in stress drop per unit time with increasing fluid pressure (Figure 3b).

The samples dilate during all stress drops. Generally, dilation initiates prior to strain weakening of the initial stress drop, with a large proportion of total dilation coinciding with the initial stress drop (Figures 2a and 2e). Dilation continues throughout apparent frictional sliding and subsequent stress drops (Figures 2b and 2f).

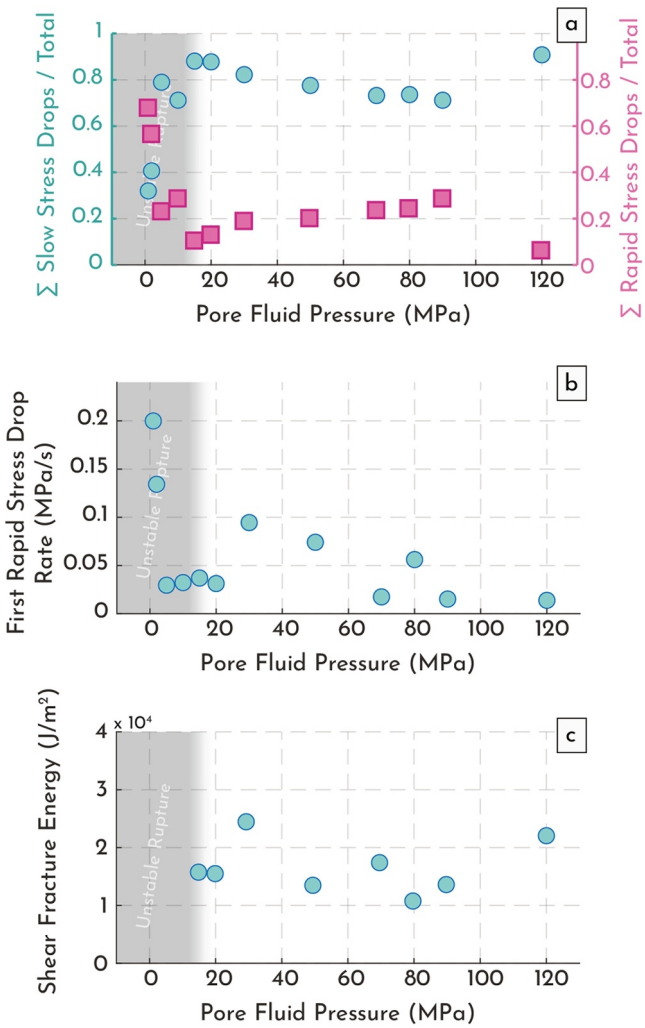

Figure 3. Patterns in stress drops with increasing pore fluid pressure (a) Cumulative sum of the slow and rapid stress drops normalized by the total stress drop, (b) The rate of stress drop during the first rapid stress drop of each experiment, (c) Shear fracture energy calculated from mechanical data.

3.2. Fracture Patterns

At the macroscopic scale, cores faulted at lower pore fluid pressures appear more localized than those faulted at higher pore fluid pressures. At low pore fluid pressures, single faults appear to accommodate the majority of shortening (Figure 4a). Cores deformed at higher pore fluid pressures exhibit more distributed fracturing, such as conjugate sets of major faults that appear to accommodate equal magnitudes of shortening (Figure 4b). Overall, there is a general increase in the number of major faults with increasing pore fluid pressure, an average of 3.7 major faults per sample at low pore fluid pressures (<15 MPa) and 4.9 major faults per sample at high pore fluid pressures (≥15 MPa) (Figure 4c).

There is not a systematic trend in the quantity or orientation of mesoscopic fractures with increasing pore fluid pressure (Figures S7 and S8 in Supporting Information S1). In general, fracture surface area increases slightly with increasing pore fluid pressure (Figure S5 in Supporting Information S1).

The greatest difference in damage occurs at the microscale. There are more than twice the number of total microcracks (3,102) in a sample faulted at high pore fluid pressure (120 MPa) than in one faulted at low pore fluid pressure (1,497, 1 MPa) (Figure 1b). At high pore fluid pressure, intragranular cracks are 126% (517 vs. 1,170) greater along radial transects and 108% (680 vs. 1,416) greater along axial transects, respectively. Transgranular cracks are also more abundant at high fluid pressure, with 89% (96 vs. 181) and 64% (204 vs. 335) more microcracks along radial and axial transects, respectively. This increase in microcracking appears to be distributed throughout the bulk sample. Transgranular microcracking, in particular, appears predominantly around major fractures at low pore fluid pressures, but much more distributed throughout the sample at high pore fluid pressures.

4. Discussion

Several aspects of the mechanical data indicate that slow failure is caused by dilatant hardening in our experiments. The slower failure process and inhibition of dynamic fault growth and slip with increasing fluid pressure occurs concomitant with sample dilation (Figure 2). This is further supported by the fact that the rate of strain weakening during the initial stress drop decreases with increasing pore fluid pressure (Figure 3b). However, structural observations show the samples are undergoing the same processes of dilation, microcrack coalescence, and fracture localization that occurs during typical brittle failure, albeit at a slower rate. Overall, our findings agree with previous studies of low-porosity crystalline rocks which show similar behaviors of fault stabilization as a result of high pore fluid pressure (Aben & Brantut, 2021, 2023; Brace & Martin, 1968; Brantut, 2020; French & Zhu, 2017; Martin, 1980). We posit that apparent frictional sliding reflects transient sliding of geometrically complex faults and not a dilatant hardening process, as evidenced by the lack of a stress drop over durations lasting minutes to hours. Periods of constant strength over such long durations have not been observed in previous studies of dilatant hardening. However, it is possible that some of our shorter duration periods of apparent frictional sliding are analogous to the stable failure events identified by Aben and Brantut (2023).

We show that the transition from dynamic to predominantly slow failure due to dilatant hardening occurs over a small range of fluid pressures between 5 and 15 MPa, above which failure behavior is relatively constant (Figure 3). We propose that below this threshold, fracture-induced dilatancy causes a complete drop in local pore fluid pressures causing pore fluids to transition from liquid to vapor. Once fluid pressure drops to zero, additional hardening is not possible and failure becomes dynamic. In contrast, at higher pore fluid pressures (≥15 MPa) the same magnitude of dilation causes pore fluid pressure to drop, but not to 0 MPa. Thus, dilatant hardening can occur throughout a stress drop and fracture propagation is inhibited. For example, at 25°C, the specific volume of

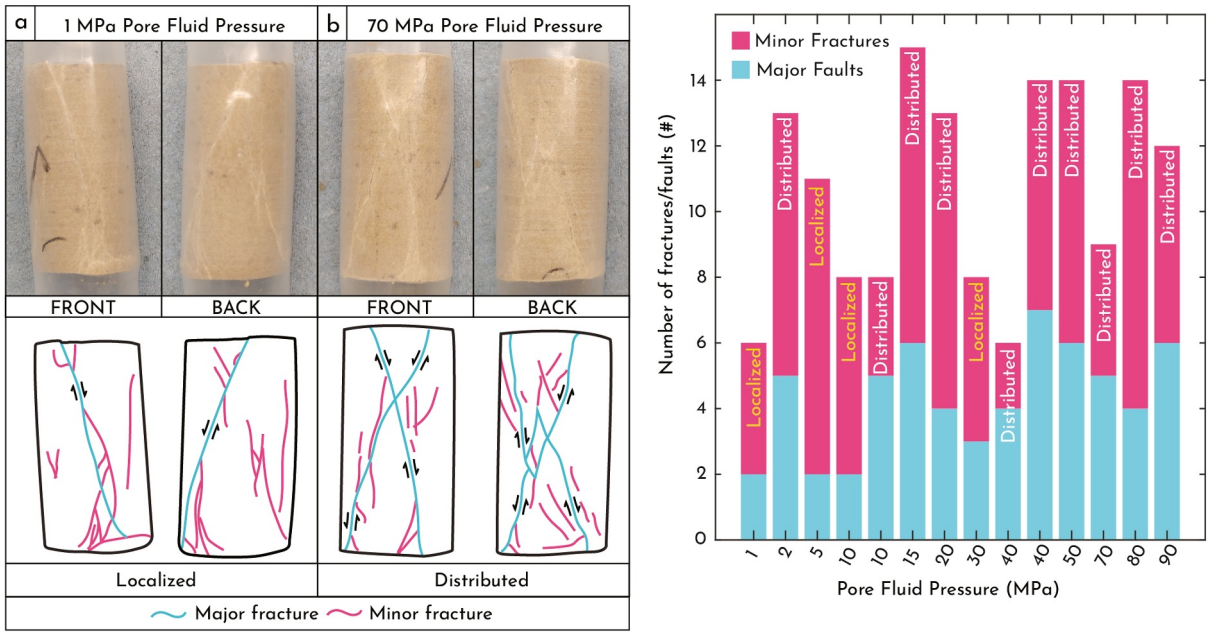

Figure 4. Macroscopic descriptions of fault patterns at different pore fluid pressures. (a) Representative sample faulted at low pore fluid pressures with a single throughgoing faults, (b) Representative sample faulted at high pore fluid pressures with a conjugate fault sets and more equal slip partitioning, (c) The number of major faults and minor fractures identified at different pore fluid pressures. A qualitative description of localized or distributed is given for each based on if there was a single throughgoing fault or distributed conjugate or complex faulting.

water increases from 0.996322 to 1.002961 cm^3/g between 15 and 0 MPa (Fine & Millero, 1973), indicating a local increase of 0.7% is required for a complete fluid pressure drop. In contrast, a pore fluid pressure drop from 70 to 0 MPa requires a 2.9% increase in local pore volume, and from 100 to 0 MPa a 4.1% increase. Our hypothesis of water vaporization at low pore fluid pressures is based on the work of Aben and Brantut (2021) who measured on-fault pore fluid pressure and showed that dynamic failure occurs when fault pore fluid pressure decreases to 0 MPa and stable failure occurs when pore fluid pressure decreases, but not completely to 0 MPa.

The transition from rapid to slow failure at pore fluid pressures below 15 MPa corresponds to stabilization at pore pressure ratios ($\lambda = P_f/\sigma_3$) greater than 0.6, which we compare with previous studies at slightly different conditions. The only other studies that evaluate stabilization at several fluid pressures were conducted on granite (Aben & Brantut, 2021; Martin, 1980), which exhibits a transition from dynamic to slow failure at $\lambda = 0.4 - 0.6$. The variability in threshold values of λ is likely the result of differences in sample porosities and characteristic dilational volumes associate with fracturing. Specifically, lower thresholds indicate lower sample porosity and/or more fracture-induced dilation, which likely varies according to lithology. This is generally consistent with our observation that the threshold for a ~3% porosity sandstone ($\lambda = 0.6$) is at the high end of values reported for granite, which tends to have porosity of ~1%. It is also consistent with the results of Martin (1980), who showed that this transition occurs at lower values of λ, with increasing effective pressure. However, more data is needed comparing microcrack dilatancy, pore structure, and porosity.

Our structural observations indicate that deformation becomes more distributed at the micro- and macroscopic scales at high pore fluid pressures where dilatant hardening slows the rate of faulting. Distributed fracturing is proposed to occur when dilatant hardening causes fracture growth to arrest due to locally low pore fluid pressure and then migrate to a region where fluid pressures are higher (French & Zhu, 2017; Figure 5). Our observations do indeed indicate that dilatant hardening results in more distributed deformation, as evidenced by higher microcrack densities and more distributed slip on faults at the macroscopic scale, although not the number of faults and mesoscopic faults.

The transition from dynamic to slow failure requires a decrease in the slope of the slip weakening curve (Figure 5) which corresponds to an increase in fracture energy (the area under the curve) with increasing fluid pressure (Martin, 1980). Unfortunately, it is not possible to document this change from mechanical data, because fracture

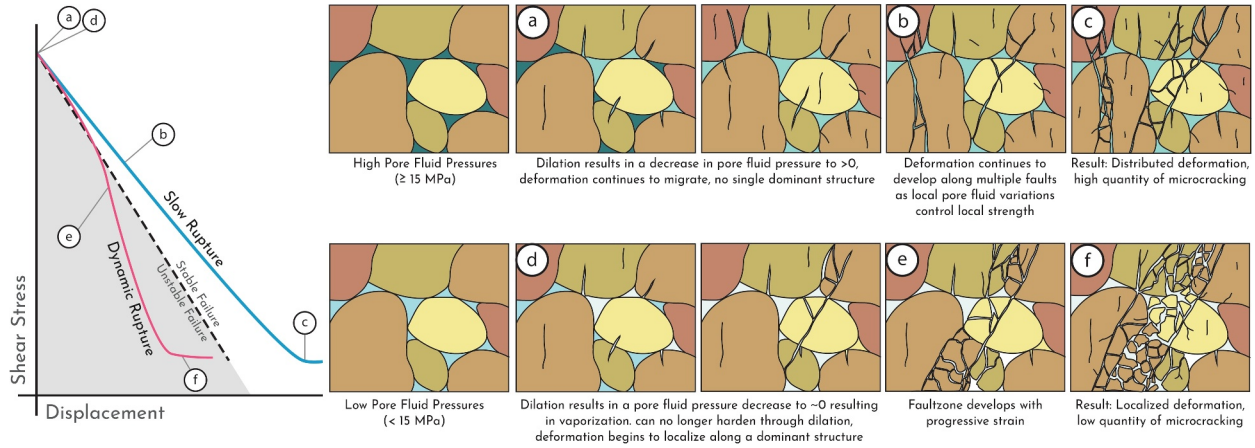

Figure 5. A conceptual structural model for the process of dilatant hardening at low and high pore fluid pressure conditions based on our observations of micro- and macrofractures. On the left is a schematic slip weakening curve by which stability is defined: the dashed line is the response of the apparatus determined by its stiffness. Stable rupture is observed when it occurs above this line, while unstable dynamic failure happens underneath. On the right is a time-evolution series for microstructures for both low and high pore fluid pressures, their corresponding progress indicated on the slip weakening curve to the left.

energy cannot be accurately quantified during dynamic failure as the slip weakening measured is the apparatus stiffness and not the rock properties. Nonetheless, the transition in behavior that we observe requires an increase in fracture energy, which we observe evidence for based on the increased microfracture densities at high fluid pressure. Our mechanical data does show that above 15 MPa pore fluid pressure fracture energy does not systematically vary during dilatant hardening (Figure 3c), as expected given the consistent hardening behavior above this threshold.

5. Implications

Our results indicate that faults may develop with variable degrees of deformation localization based on λ, whereby dilatant hardening can influence microfracture densities and whether slip occurs on a single fault or across multiple faults. Our observations are consistent with more limited documentation of deformation distribution in serpentinite (French & Zhu, 2017), indicating the structural effects of dilatant hardening are not strongly dependent on lithology. Thus, we expect that these processes may be reflected in the rock record as zones of distributed deformation where fault slip and dilation is more equally distributed between neighboring structures as opposed to single localized deformation (Figure 5).

The dynamics of slip along natural faults will depend on a loss of cohesion that is smaller than our intact samples and the stiffness of the natural system; however, our results provide important insights into the processes controlling dilatant hardening. We and previous studies show that stabilization in the lab can occur at values of $\lambda \approx 0.6$, which is well-below the near-lithostatic pore fluid pressures inferred at geologic settings where slow slip and high pore fluid pressures are interpreted to coincide (Audet et al., 2009; Liu & Rice, 2007; Peacock et al., 2011; Shelly et al., 2006), indicating that the process is likely active and increases fracture energy of fault slip in geologic settings where slow slip is observed.

6. Conclusions

We document the mechanical and structural impacts of dilatant hardening during loss of cohesion in a low-porosity sandstone, to constrain the processes driving this phenomenon in fault zones. Our results show a transition in mechanical behavior at fluid pressure ratios less than $\lambda = 0.6$, above which dilatancy stabilizes failure and the resulting deformation is relatively insensitive to fluid pressure. Observations of stable slip correlate to significant structural observations that inform the deformation process. At the macroscopic scale, stable failure coincides with more equivalent fault development and slip distributions between major faults, and at the microscopic scale microcracking increases by a factor of 2. Thus, dilatant hardening has the potential to change the dynamics of slip through increased fracture energy while also being recorded in the structures of fault rocks.

Data Availability Statement

Processed data for each experiment and corresponding CT-image data sets on which this article is based on are available in Williams and French (2024).

Acknowledgments
This work was funded by NSF EAR #1759127 to MEF. The authors also thank Jess McBeck and an anonymous reviewer for their detailed feedback which significantly improved this manuscript.

References

Aben, F. M., & Brantut, N. (2021). Dilatancy stabilises shear failure in rock. *Earth and Planetary Science Letters*, *574*, 117174. https://doi.org/10.1016/j.epsl.2021.117174

Aben, F. M., & Brantut, N. (2023). Rupture and afterslip controlled by spontaneous local fluid flow in crustal rock. *Journal of Geophysical Research: Solid Earth*, *128*(11), 1–14. https://doi.org/10.1029/2023JB027534

Audet, P., Bostock, M. G., Christensen, N. I., & Peacock, S. M. (2009). Seismic evidence for overpressured subducted oceanic crust and megathrust fault sealing. *Nature*, *457*(7225), 76–78. https://doi.org/10.1038/nature07650

Brace, W. F. (1978). Volume changes during fracture and frictional sliding: A review. *Pure and Applied Geophysics*, *116*(4–5), 603–614. https://doi.org/10.1007/BF00876527

Brace, W. F., & Martin, R. J. (1968). A test of the law of effective stress for crystalline rocks of low porosity. *International Journal of Rock Mechanics and Mining Sciences*, *5*(5), 415–426. https://doi.org/10.1016/0148-9062(68)90045-4

Brace, W. F., Paulding, B. W., & Scholz, C. (1966). Dilatancy in the fracture of crystalline rocks. *Journal of Geophysical Research*, *71*(16), 3939–3953. https://doi.org/10.1029/jz071i016p03939

Brantut, N. (2020). Dilatancy-induced fluid pressure drop during dynamic rupture: Direct experimental evidence and consequences for earthquake dynamics. *Earth and Planetary Science Letters*, *538*, 1–23. https://doi.org/10.1016/j.epsl.2020.116179

Ceia, M., Missagia, R., Fasolo, R., & Neto, I. (2019). Relationship between porosity, permeability and pore compressibility. In *Proceedings of the 16th International Congress of the Brazilian Geophysical Society & ExpoGEf, August* (pp. 1–6). https://doi.org/10.22564/16cisbgf2019.287

Churcher, P. L., French, P. B., Shaw, J. C., & Schramm, L. L. (1991). Rock properties of Berea sandstone, Baker dolomite, and Indiana limestone. In *Proceedings of SPE International Symposium on Oilfield Chemistry, January* (pp. 431–446). https://doi.org/10.2523/21044-ms

Fine, R. A., & Millero, F. J. (1973). Compressibility of water as a function of temperature and pressure. *The Journal of Chemical Physics*, *59*(10), 5529–5536. https://doi.org/10.1063/1.1679903

Frank, F. C. (1965). On dilatancy in relation to seismic sources. *Review of Geophysics*, *3*(4), 485–503. https://doi.org/10.1029/rg003i004p00485

French, M. E., & Zhu, W. (2017). Slow fault propagation in serpentinite under conditions of high pore fluid pressure. *Earth and Planetary Science Letters*, *473*, 131–140. https://doi.org/10.1016/j.epsl.2017.06.009

Gehne, S., & Benson, P. M. (2017). Permeability and permeability anisotropy in crab orchard sandstone: Experimental insights into spatio-temporal effects. *Tectonophysics*, *712–713*, 589–599. https://doi.org/10.1016/j.tecto.2017.06.014

Handin, J., Hager, R. V., Friedman, M., & Feather, J. N. (1963). Experimental deformation of sedimentary rocks under confining pressure: Pore pressure tests. *AAPG Bulletin*, *47*(5), 717–755. https://doi.org/10.1306/bc743a87-16be-11d7-8645000102c1865d

Liu, Y., & Rice, J. R. (2007). Spontaneous and triggered aseismic deformation transients in a subduction fault model. *Journal of Geophysical Research*, *112*(9), 1–23. https://doi.org/10.1029/2007JB004930

Liu, Y., & Rubin, A. M. (2010). Role of fault gouge dilatancy on aseismic deformation transients. *Journal of Geophysical Research*, *115*(10), 1–23. https://doi.org/10.1029/2010JB007522

Martin, R. J. (1980). Pore pressure stabilization of failure in westerly granite. *Geophysical Research Letters*, *7*(5), 404–406. https://doi.org/10.1029/gl007i005p00404

Menéndez, B., Zhu, W., & Wong, T. F. (1996). Micromechanics of brittle faulting and cataclastic flow in Berea sandstone. *Journal of Structural Geology*, *18*(1), 1–16. https://doi.org/10.1016/0191-8141(95)00076-P

Ougier-Simonin, A., & Zhu, W. (2013). Effect of pore fluid pressure on slip behaviors: An experimental study. *Geophysical Research Letters*, *40*(11), 2619–2624. https://doi.org/10.1002/grl.50543

Peacock, S. M., Christensen, N. I., Bostock, M. G., & Audet, P. (2011). High pore pressures and porosity at 35 km depth in the Cascadia Subduction Zone. *Geology*, *39*(5), 471–474. https://doi.org/10.1130/G31649.1

Rice, J. R. (1975). On the stability of dilatant hardening for saturated rock masses. *Journal of Geophysical Research*, *80*(11), 1531–1536. https://doi.org/10.1029/jb080i011p01531

Rudnicki, J. W. (1984). Shear deformation in fissured rock masses. *Journal of Geophysical Research B*, *89*(811), 9259–9270. https://doi.org/10.1029/jb089ib11p09259

Segall, P., Rubin, A. M., Bradley, A. M., & Rice, J. R. (2010). Dilatant strengthening as a mechanism for slow slip events. *Journal of Geophysical Research*, *115*(12), 1–37. https://doi.org/10.1029/2010JB007449

Shelly, D. R., Beroza, G. C., Ide, S., & Nakamula, S. (2006). Low-frequency earthquakes in Shikoku, Japan, and their relationship to episodic tremor and slip. *Nature*, *442*(7099), 188–191. https://doi.org/10.1038/nature04931

Williams, S. A., & French, M. E. (2024). Experimental datasets and CT-images for dilatant hardening study - Williams and French 2024 [Dataset]. https://doi.org/10.5281/zenodo.10656036

Zhu, W., Allison, K. L., Dunham, E. M., & Yang, Y. (2020). Fault valving and pore pressure evolution in simulations of earthquake sequences and aseismic slip. *Nature Communications*, *11*(1), 1–11. https://doi.org/10.1038/s41467-020-18598-z

References From the Supporting Information

Mavko, G., Mukerji, T., & Dvorkin, J. (2009). Rock physics handbook (2nd ed., Vol. *4*, No. (1)).

Otsu, N. (1979). A threshold selection method from gray-level histograms. *SMC*, *9*(1), 62–66. https://doi.org/10.1109/tsmc.1979.4310076

Wong, T.-F. (1982). Shear fracture energy of westerly granite from post-failure behavior. *Journal of Geophysical Research*, *87*(B2), 990–1000. https://doi.org/10.1029/jb087ib02p00990